

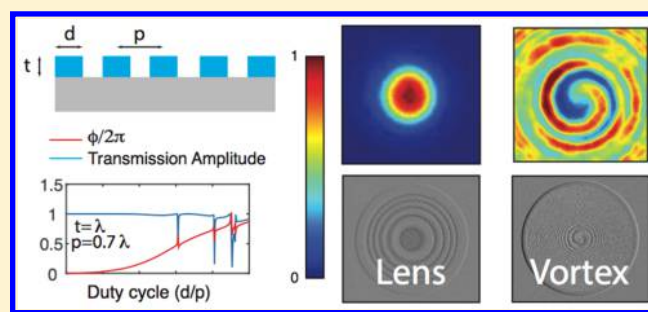
## Low-Contrast Dielectric Metasurface Optics

Alan Zhan,<sup>†</sup> Shane Colburn,<sup>‡</sup> Rahul Trivedi,<sup>§</sup> Taylor K. Fryett,<sup>‡</sup> Christopher M. Dodson,<sup>‡</sup> and Arka Majumdar<sup>\*,†,‡</sup><sup>†</sup>Department of Physics and <sup>‡</sup>Department of Electrical Engineering, University of Washington, Seattle, Washington 98122, United States<sup>§</sup>Department of Electrical Engineering, Indian Institute of Technology, Delhi 110016, India

## Supporting Information

**ABSTRACT:** The miniaturization of current image sensors is largely limited by the volume of the optical elements. Using a subwavelength-patterned quasi-periodic structure, also known as a metasurface, one can build planar optical elements based on the principle of diffraction. Recent demonstrations of high-quality metasurface optical elements are mostly based on high-refractive-index materials. Here, we present a design of low-contrast metasurface-based optical elements. We fabricate and experimentally characterize several silicon nitride-based lenses and vortex beam generators. The fabricated lenses achieved beam spots of less than 1  $\mu\text{m}$  with numerical apertures as high as  $\sim 0.75$ . We observed a transmission efficiency of 90% and focusing efficiency of 40% in the visible regime. Our results pave the way toward building low-loss metasurface-based optical elements at visible frequencies using low-contrast materials and extend the range of prospective material systems for metasurface optics.

**KEYWORDS:** diffractive optics, dielectric metasurface, silicon nitride photonics, lens, vortex beam generator



Conventional transmissive macroscopic optical elements primarily depend on refraction to control light propagation. Refraction relies heavily upon the exact curvature of the surface and the spatial extent of the element in order to achieve gradual phase accumulation. This imposes a fundamental limitation on the miniaturization of optical sensors and elements, which is necessary for various applications such as the Internet of Things,<sup>1</sup> biophotonics,<sup>2,3</sup> and two-photon absorption microscopy.<sup>4</sup> Metasurfaces, two-dimensional quasi-periodic arrays of subwavelength structures, present a novel method of miniaturizing optical elements. Rather than relying on gradual phase accumulation through light propagation, each subwavelength structure imparts a discrete, abrupt change in the phase of incoming light.<sup>5–8</sup> This has motivated the design of metasurface-based optical elements including lenses,<sup>9,10</sup> focusing mirrors,<sup>11</sup> vortex beam generators,<sup>12,13</sup> holographic masks,<sup>14–16</sup> and polarization optics.<sup>17,18</sup>

Thus far, high-quality metasurface optical elements based on metals,<sup>6,19</sup> titanium oxide,<sup>20,21</sup> and amorphous silicon<sup>22,23</sup> have been demonstrated. Unfortunately, metals are significantly lossy at optical frequencies,<sup>24</sup> titanium oxide is CMOS incompatible, and amorphous silicon absorbs light in the visible and near-infrared spectrum ( $\sim 400$ – $900$  nm). This wavelength range is of particular interest for many applications due to ubiquitous, low-cost silicon detectors, motivating the development of high-band-gap material based metasurfaces. However, high-band-gap CMOS-compatible materials such as silicon nitride and silicon dioxide, which are transparent over the aforementioned

wavelength range, have a low refractive index. Although silicon dioxide metasurface lenses have been previously demonstrated, they had low numerical apertures, resulting in large beam spots.<sup>25,26</sup> In this paper, we demonstrate operation of high-quality metasurface lenses ( $\text{NA} \approx 0.75$ ) and vortex beam generators based on silicon nitride at visible wavelengths. Our results present a methodology for producing low-loss, high-quality metasurface optics that are compatible with both silicon detectors and conventional CMOS fabrication technologies.

The main building block of a metasurface is a grating composed of scatterers arranged in a subwavelength periodic lattice (with a period  $p$ ). In this paper, we focus on cylindrical posts as the scatterers, which are arranged on a square lattice (Figure 1a). For such a grating, the higher order diffracted plane waves are evanescent, and only the zeroth-order plane wave propagates a significant distance from the grating.<sup>27</sup> The complex transmission coefficient of this plane wave depends upon the grating periodicity  $p$ , scatterer dimensions (both the diameter  $d$  and thickness  $t$ ), and refractive index  $n$ , as shown in Figure 1. The use of metasurfaces to build optical components is primarily motivated by the observation that the functionality of many such components, such as lenses and focusing mirrors, is determined by a spatial phase profile imparted on an incident beam. Reproducing these devices using a metasurface involves selecting the correct parameters to achieve the desired spatial

Received: November 16, 2015

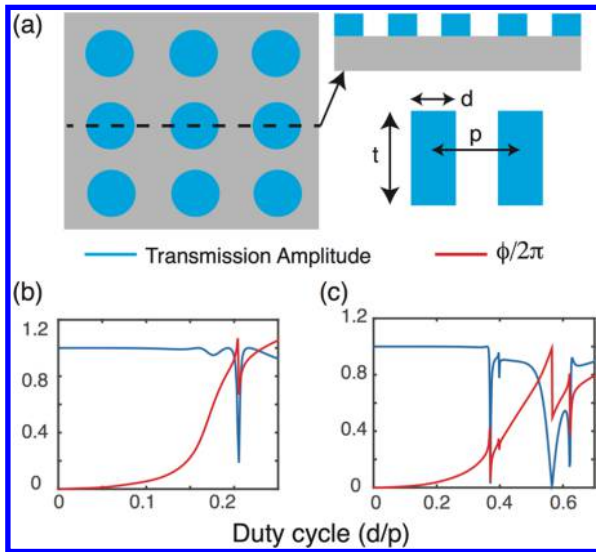


**Figure 1.** Low- and high-contrast metasurfaces. (a) Schematic of the grating structures: a grating with periodicity  $p$  can be formed by using cylindrical posts (with diameter  $d$ ) arranged in a square lattice. The thickness of the grating is denoted as  $t$ . Amplitude and phase  $\phi$  of the transmitted light for (b) a high contrast ( $n_{\text{high}} = 3.5$ ) with thickness  $t = 0.7\lambda$  and periodicity  $p = 0.52\lambda$ . (c) Low-contrast ( $n_{\text{low}} = 2.0$ ) grating using parameters from (b) scaled by  $n_{\text{high}}/n_{\text{low}}$  resulting in final parameters  $t = 1.05\lambda$  and  $p = 0.91\lambda$ .

phase profile, arranging the scatterers on a subwavelength lattice, and spatially varying their dimensions. To design an arbitrary transmission phase profile, we must be capable of producing phase shifts spanning the whole  $0$  to  $2\pi$  range while maintaining large transmission amplitudes. Such phase variations have been demonstrated earlier with high refractive

index scatterers (Figure 1b). Via numerical simulation using rigorous coupled-wave analysis (RCWA),<sup>26</sup> we found that it is possible to select parameters to achieve such a phase variation with a low contrast grating. In these simulations, we calculate the achievable phases and transmission amplitudes by varying the diameter  $d$  of the posts for a fixed periodicity  $p$ , substrate thickness ( $t_{\text{sub}} = \lambda$ ), and refractive index of  $n \approx 2$ . A possible procedure to obtain a low-contrast grating design is to simply scale the high-contrast grating inversely with the refractive index. However, while such a simple scaling method can produce phase shifts spanning the whole  $0$  to  $2\pi$  range, it also results in severe dips in the transmission amplitude due to the appearance of resonances (Figure 1c). Note that these resonances also appear in the high-contrast case (Figure 1b), but they are generally significantly narrower when compared to the low-contrast case. The broad resonances in the low-contrast design result in strongly varying transmission amplitudes, rendering it unsuitable for an efficient optical element.

These resonances can be engineered by choosing different grating parameters, such as thickness and periodicity. Specifically, by varying the thickness and periodicity of the low contrast grating, we can transition from a region with many resonances to a nonresonant regime. Simulation results with varied thicknesses and periodicities are shown in Figure 2. For  $t = 1.2\lambda$  and  $p = 0.4\lambda$ , both the phase delay and transmission amplitude are continuous for all the simulated post diameters, with only small variations in the transmission amplitude (Figure 2k). This set of parameters can be considered to be fully within the nonresonant regime, as it lacks any discontinuities in the phase or transmission amplitude. Unfortunately, this design has a large aspect ratio, making it difficult to fabricate. By increasing the thickness of the pillars, the resonances are narrowed for a given periodicity (Figure 2). Additionally, increasing the periodicity for a fixed thickness results in more resonances in

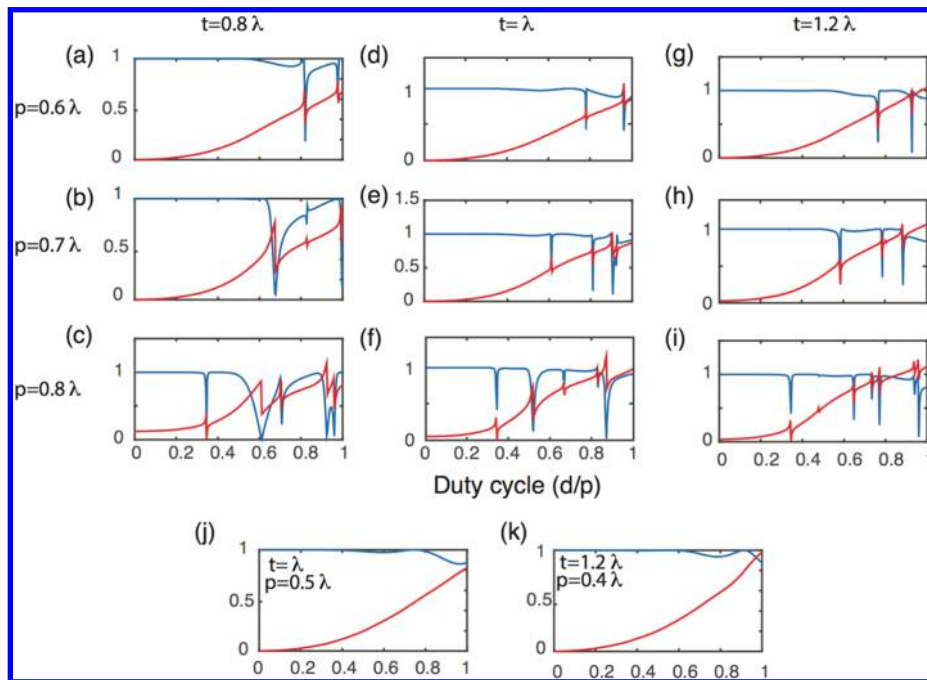


**Figure 2.** Amplitude and phase of the transmitted light through low-contrast metasurfaces with different duty cycles, periodicities, and thicknesses. (j) and (k) represent low contrast parameter sets that lack resonances altogether. Plotted are phase delays (red) and transmission amplitudes (blue) for gratings as a function of the duty cycles for varied periodicity and thickness. We find that in increasing the thickness of the pillars, the resonances are narrowed for a given periodicity. On the other hand, increasing the periodicity for a fixed thickness results in more resonances in all cases.

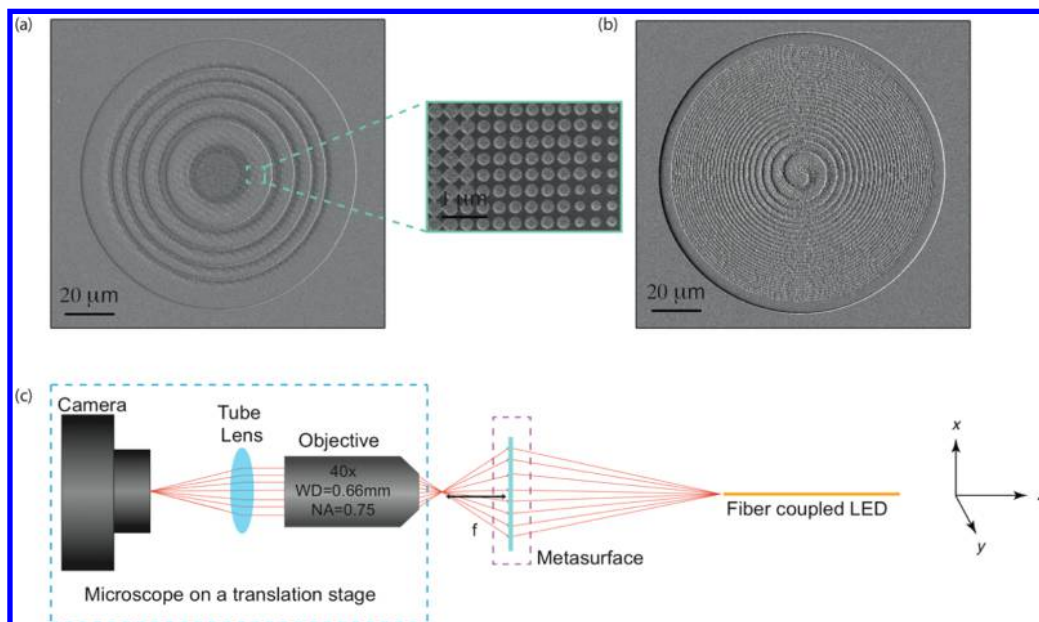


**Figure 3.** Metasurface lens and setup. (a) Scanning electron micrograph (SEM) of a  $f = 0.5$  mm lens. Zoom shows aluminum-capped silicon nitride pillars arranged on a square lattice. (b) SEM of a focusing vortex beam generator with  $l = 1$  and  $f = 100$   $\mu\text{m}$ . (c) Microscopy setup for imaging the focal plane. The microscope can be translated along the optical axis.

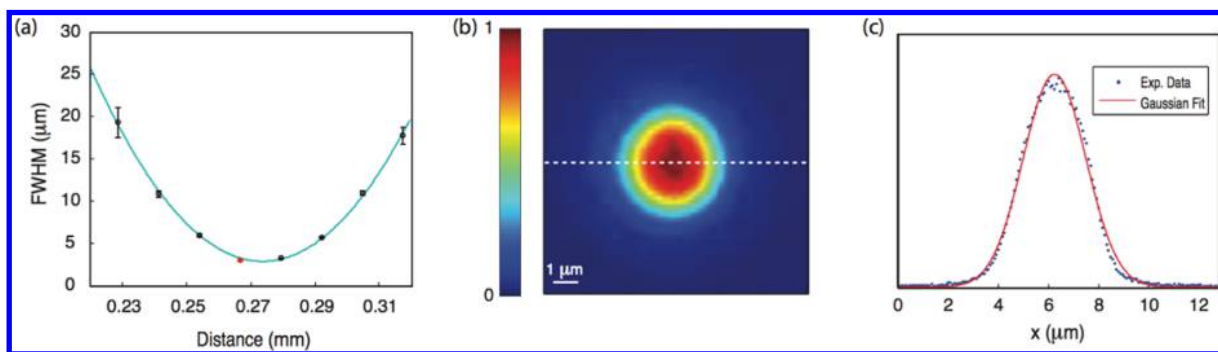


**Figure 4.** Focal length lens ( $250$   $\mu\text{m}$ ) performance measured with an LED centered at  $626$  nm. (a) The fwhm is plotted as a function of the distance in the  $z$ -direction. The working distance of the objective has been subtracted. The error bars denote the 95% confidence interval for the Gaussian fits. The blue curve is a guide to the eye. (b) 2D intensity profile at the focal plane, the red point in (a). (c) A Gaussian function is fit to the cross-section data to estimate the beam size. Cross-section is taken from dashed white line in (c). We use the fwhm as a measure of the beam size.

all cases (Figure 2). On the basis of these simulations, we chose the parameters  $t = \lambda$  and  $p = 0.7\lambda$  (Figure 2e), to ensure a moderate aspect ratio for fabrication while maintaining near-unity transmission amplitudes for the whole range of phases.

With this design in hand, we can realize arbitrary phase profiles by arranging these scatterers on a lattice. We chose to fabricate aspheric lenses and a vortex beam generator due to their relatively simple phase profiles. The spatial phase profile of a lens is given by

$$\Phi(x, y) = \frac{2\pi}{\lambda}(\sqrt{x^2 + y^2 + f^2} - f) \quad (1)$$

where  $f$  is the focal length of the lens,  $(x, y)$  are the in-plane coordinates,  $z$  is the propagation direction, and  $\lambda$  is the design wavelength. The spatial phase profile of a focusing vortex beam generator is

$$\Phi(x, y) = \frac{2\pi}{\lambda}(\sqrt{x^2 + y^2 + f^2} - f) + l\theta \quad (2)$$

which is a lens modified by the angular momentum term ( $l\theta$ ), where  $l$  is an integer specifying the orbital angular momentum

state and  $\theta$  is the azimuthal angle in the lens plane. In our design, we first discretize the continuous spatial phase profile onto a square lattice with periodicity  $p$ , giving us a discrete spatial phase map with many different phase values. We then choose to approximate the discrete phase profile with six linear steps between  $0$  and  $2\pi$ , corresponding to six different pillar radii. For each value of this new discrete spatial phase profile, we find the radius of the pillar that most closely reproduces that phase and place it on the lattice. In all of our devices, we choose a design wavelength of  $633$  nm, which corresponds to a thickness of  $633$  nm ( $\lambda$ ), periodicity of  $443$  nm ( $0.7\lambda$ ), and pillar radii that vary from  $96$  to  $221$  nm when using the parameters given in Figure 2e.

We fabricated and characterized metasurface lenses and vortex beam generators in silicon nitride ( $n \approx 2$ ). Figure 3a and b show a scanning electron micrograph (SEM) of the fabricated lens and a vortex beam generator, respectively. We prepared the wafer by depositing  $633$  nm of silicon nitride on a  $500$   $\mu\text{m}$  thick quartz substrate using plasma-enhanced chemical vapor deposition (PECVD). Aluminum ( $50$  nm) was then evaporated onto the silicon nitride, serving both as a hard mask and as a

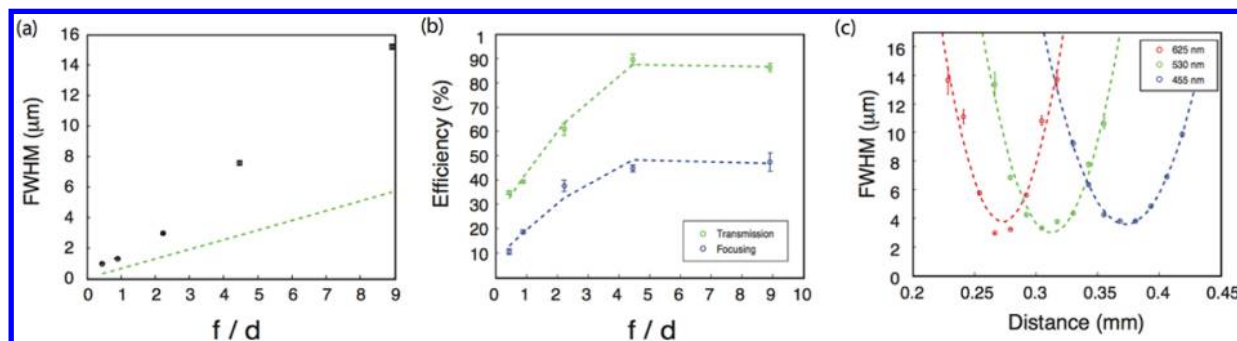


**Figure 5.** Performance of metasurface lenses plotted as a function of the ratio of their focal length to diameter  $f/d$ . (a) Measured focal spot sizes for all fabricated lenses. The dashed green line is the diffraction-limited fwhm. The justification for the green line is shown in [supplement S1](#). (b) Measured transmission and focusing efficiencies for all fabricated lenses. Error bars are obtained from the standard deviation of three measurements on each device. (c) Chromatic dispersion of the  $250\ \mu\text{m}$  lens. Red, blue, and green correspond to illumination with 625, 530, and 455 nm LEDs, respectively. Plotted curves are a guide to the eye, and error bars represent the 95% confidence intervals for the Gaussian fits.

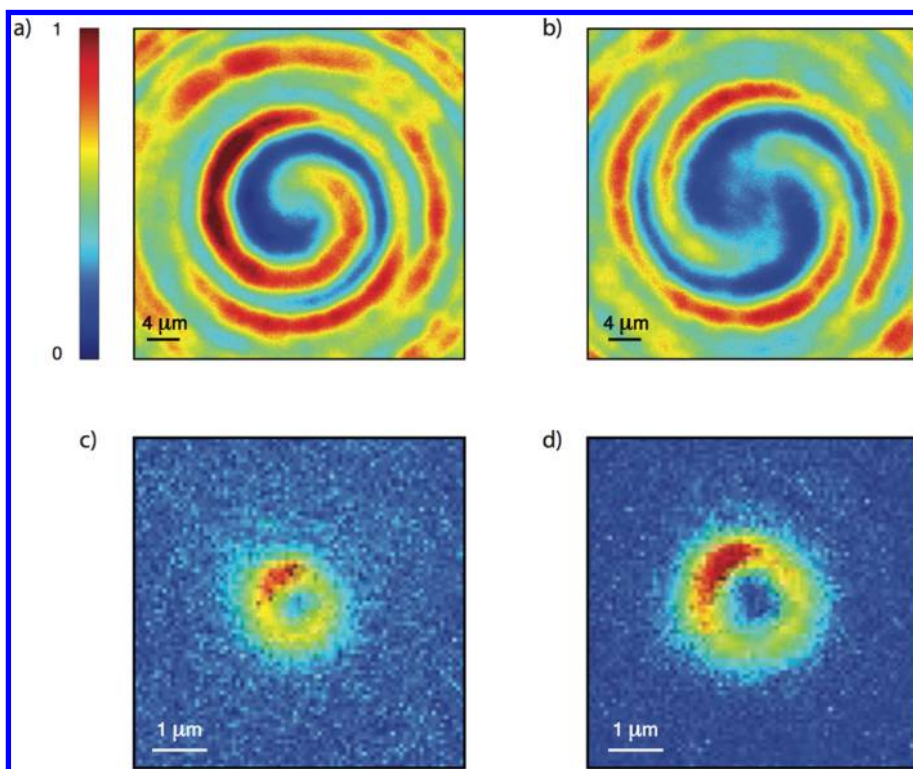


**Figure 6.** Vortex beam generator field profiles. The normalized intensity profiles for  $l = 1$  showing the (a) helical wavefront with one curl and the (c) characteristic donut intensity distribution. (b and d) Helical wavefront with two curls and the characteristic donut intensity profile for  $l = 2$ , respectively. All of the figures share the same color bar.

charge-dissipation layer necessary for electron-beam lithography. The pattern was exposed on 160 nm ZEP 520A using a Jeol JBX-6300FS 100 kV electron-beam lithography system. Following development in amyl acetate, the sample was dry etched with a  $\text{Cl}_2$  and  $\text{BCl}_3$  plasma to transfer the pattern on the aluminum layer, forming the hard mask. Finally, a  $\text{CHF}_3$  and  $\text{O}_2$  plasma was used to etch the 633 nm pillars, and the remaining aluminum was removed with sulfuric acid.

The schematic of the optical setup used to probe the structures is shown in [Figure 3c](#). The characterization setup utilizes a  $40\times$  objective (Nikon Plan Fluor) with a working distance of 0.66 mm and NA 0.75 and a tube lens (Thorlabs SM2A20) with a focal length of 20 cm as a microscope. The magnification of the setup was determined using known dimensions of the lens. We mount the metasurface on a glass

slide with the front facing the microscope. The devices were illuminated with red (Thorlabs M625F1), green (Thorlabs M530F1), and blue (Thorlabs M455F1) light-emitting diodes (LEDs).

The intensity profiles were captured using the microscope and a Point Grey Chameleon camera. By translating the microscope and camera along the optical axis, we can move into and out of the focal plane and image the  $x$ - $y$  plane intensity profile at varying  $z$ -distances. During characterization we can clearly see that the beam radius is changing as we translate into and out of the focus. The full-width at half-maxima (fwhm) values obtained by a Gaussian fit are plotted in [Figure 4a](#) as a function of the distance in the  $z$ -direction. The increasing error bars away from the focal distance are due to the divergence of the single peak into two peaks as the microscope moves out of

the focal plane. A typical example of the intensity profile near the focal point is shown in Figure 4b. A Gaussian fit is shown in Figure 4c.

We fabricated lenses with five different focal lengths between 50  $\mu\text{m}$  and 1 mm with a lens radius of 56  $\mu\text{m}$ . The measured fwhm's of the focal spot sizes for all the lenses are plotted against the ratio of the lens focal length ( $f$ ) to lens diameter ( $d$ ) in Figure 5a, where the dotted green line is the fwhm of a diffracted-limited spot of a lens with the given geometric parameters. The deviation from the diffraction limit is attributed mostly to fabrication imperfection. The criterion for the diffraction-limited fwhm spot is given in supplement S1, and simulated spot sizes for low  $f/d$  lenses are provided in supplement S2. The 50  $\mu\text{m}$  lens achieves a fwhm less than 1  $\mu\text{m}$ . The measurement of the focal distance also agrees well with our design parameters.

In order to measure the focusing efficiency of the lens, we inserted a flip mirror before the camera to direct the beam to a power meter (Newport 1918-R). We then measure the incident power to the focus by using a pinhole to isolate a spot with radius 3 times the fwhm. The focusing efficiency was taken to be the ratio of the power incident on the focus to the power incident on the lens. The transmission efficiency was taken to be the ratio of the power incident on the detector through the lens to the power incident through a glass slide. Transmission and focusing efficiencies both show an increase as the focal length of the lens increases, as shown in Figure 5b. The focusing efficiency reaches a maximum of  $\sim 40\%$  for the 1 mm lens, and the transmission efficiency rises to near 90% for the 500  $\mu\text{m}$  lens. These transmission efficiencies are significantly higher than other metasurfaces in the visible frequency range.<sup>15,23,28</sup> Simulated efficiencies for both low- and high-contrast lenses with low  $f/d$  are provided in supplement S2. In addition, we investigated the chromatic behavior of the lens for red, green, and blue light. The wavelength dependence of the 250  $\mu\text{m}$  focal length lens is shown in Figure 5c. The focal distance of our lens increases with decreasing wavelength, increasing from  $\sim 0.26$  mm at 625 nm to  $\sim 0.35$  mm at 455 nm. We also observe an increase in the size of the focal spot with decreasing wavelength, from a minimum of  $\sim 3$   $\mu\text{m}$  at 625 nm to a maximum of  $\sim 4$   $\mu\text{m}$  at 455 nm. We remark that the product of the experimentally measured focal length ( $f$ ) and illumination wavelength ( $\lambda$ ) is roughly constant for our design, as expected for diffraction-based optics.<sup>29</sup>

Finally, we characterized the vortex beam generators and imaged their intensity profiles as shown in Figure 6a–d. They were all fabricated for a design wavelength of 633 nm, focal lengths of 100  $\mu\text{m}$ , radius of 60  $\mu\text{m}$ , and orbital angular momentum states  $l = 1$  (Figure 5a,c), and  $l = 2$  (Figure 5b,d). The experimentally measured spiral intensity and the characteristic donut profiles clearly show the two distinct orbital angular momentum states. The intensity profiles were taken using the same setup as the lenses using a 625 nm LED. The spiral profiles were taken at a point off of the focal plane. As expected, the  $l = 1$  spiral profile has only one curl, while the  $l = 2$  profile has two. Both spirals also curl along the same direction, indicating they are of the same parity. In order to image the donut profiles, the microscope was translated into the focal plane of the vortex beam generator. Comparing the donut profiles, the higher angular momentum beam has a larger donut radius, which is consistent with the behavior of the higher order Laguerre–Gauss modes.<sup>30</sup> The transmission efficiencies of the vortex beam generators are measured in the same manner as

those of the lenses. For the focusing efficiency, we isolate the power concentrated into the donut field intensity profile at the focal plane using a pinhole. Both of the devices show transmission efficiencies of up to 80% and focusing efficiencies of around 10%. These devices show higher transmission efficiencies and lower focusing efficiencies than those of a similar lens fabricated for a 100  $\mu\text{m}$  focal length, which had transmission and focusing efficiencies of around 40% and 20%, respectively. We attribute this to the fabrication of the vortex beam generator, as its phase profile results in a higher pillar radius gradient, which is difficult to realize in fabrication. In our case, this resulted in the overexposure and ultimately overetching of the pillars. We posit that the overetching would allow more incoming light to pass through undiffracted, increasing the transmission efficiency of the device. However, this would also decrease the focusing efficiency as less incoming light is diffracted toward the focal point.

We have designed and fabricated low-contrast high-quality metasurface optical elements based on silicon nitride. Our lenses achieved transmission efficiencies of up to 90% and focusing efficiencies of up to 40%, in addition to a sub 1  $\mu\text{m}$  spot size, with a numerical aperture of 0.75. The performance of these lenses is significantly better than previously reported results in the context of low-contrast diffractive gratings. Recent demonstration of optical elements with similar performance employed high-contrast materials such as metals and silicon that are incompatible with operation in the visible spectrum. The formalism we developed is applicable for the design of arbitrary spatial phase profiles in the same way as previous designs and brings the field of metasurface optics fully into the visible spectrum. Additionally, by using silicon nitride as our metasurface material, we can leverage both CMOS compatibility and low visible absorption to design our lenses. We emphasize that our analysis is not limited to silicon nitride ( $n \approx 2$ ), but is also applicable to other low-index materials such as transparent conducting oxides (TCO), organic polymers, transparent printable materials, and silicon dioxide. These materials, specifically TCOs and organic polymers, may provide an easier way to tune the metasurface elements due to their stronger electro-optic properties<sup>31–34</sup> and strong free carrier dispersion.<sup>35</sup>

In conclusion, we have demonstrated a low-contrast metasurface design allowing for the arbitrary shaping of an optical wavefront in the visible regime. The use of low-contrast materials extends the range of materials available for metasurface optics. The wavelength-scale thickness and planar geometry of the optical elements allows the miniaturization of optical elements for integration on optical fibers for biophotonics and use in small-scale optical systems. In addition, this approach greatly simplifies the design and fabrication process of complicated aspherical optical elements, including free-form optics.<sup>36</sup>

## ■ ASSOCIATED CONTENT

### 📄 Supporting Information

The Supporting Information is available free of charge on the ACS Publications website at DOI: 10.1021/acsp Photonics.5b00660.

A criterion for diffraction-limited lenses, FDTD simulations of achievable spot sizes, efficiencies for low- and high-contrast lenses, and angular incidence behavior (PDF)

## AUTHOR INFORMATION

## Corresponding Author

\*E-mail: arka@uw.edu.

## Notes

The authors declare no competing financial interest.

## ACKNOWLEDGMENTS

We would like to thank Dr. Andrei Faraon for useful discussions. All of the fabrication was performed at the Washington Nanofabrication Facility (WNF), a National Nanotechnology Infrastructure Network (NNIN) site at the University of Washington, which is supported in part by the National Science Foundation (awards 0335765 and 1337840), the Washington Research Foundation, the M. J. Murdock Charitable Trust, GCE Market, Class One Technologies, and Google. The research work is supported by the startup fund provided by University of Washington, Seattle, and Intel Early Career Faculty Award.

## REFERENCES

- (1) Gill, P. Enabling a Computer to Do the Job of a Lens. *SPIE* **2013**, DOI: 10.1117/2.1201309.005108.
- (2) Wilt, B. A.; Burns, L. D.; Ho, E. T. W.; Ghosh, K. K.; Mukamel, E. A.; Schnitzer, M. J. Advances in Light Microscopy for Neuroscience. *Annu. Rev. Neurosci.* **2009**, *32*, 435.
- (3) Ghosh, K. K.; Burns, L. D.; Cocker, E. D.; Nimmerjahn, A.; Ziv, Y.; Gamal, A. E.; Schnitzer, M. J. Miniaturized Integration of a Fluorescence Microscope. *Nat. Methods* **2011**, *8*, 871–878.
- (4) Helmchen, F.; Denk, W. Deep Tissue Two-Photon Microscopy. *Nat. Methods* **2005**, *2*, 932–940.
- (5) Genevet, P.; Yu, N.; Aieta, F.; Lin, J.; Kats, M. A.; Blanchard, R.; Scully, M. O.; Gaburro, Z.; Capasso, F. Ultra-Thin Plasmonic Optical Vortex Plate Based on Phase Discontinuities. *Appl. Phys. Lett.* **2012**, *100*, 013101.
- (6) Yu, N.; Capasso, F. Flat Optics with Designer Metasurfaces. *Nat. Mater.* **2014**, *13*, 139–150.
- (7) Kildishev, A. V.; Boltasseva, A.; Shalaev, V. M. Planar Photonics with Metasurfaces. *Science* **2013**, *339*, 1232009. DOI: 10.1126/science.1232009.
- (8) Monticone, F.; Estakhri, N. M.; Alù, A. Full Control of Nanoscale Optical Transmission with a Composite Metascreen. *Phys. Rev. Lett.* **2013**, *110*, 203903.
- (9) Arbabi, A.; Horie, Y.; Ball, A. J.; Bagheri, M.; Faraon, A. Subwavelength-Thick Lenses with High Numerical Apertures and Large Efficiency Based on High-Contrast Transmitarrays. *Nat. Commun.* **2015**, *6*, 706910.1038/ncomms8069.
- (10) Vo, S.; Fattal, D.; Sorin, W. V.; Zhen, P.; Tho, T.; Fiorentino, M.; Beausoleil, R. G. Sub-Wavelength Grating Lenses with a Twist. *IEEE Photonics Technol. Lett.* **2014**, *26*, 1375–1378.
- (11) Fattal, D.; Li, J.; Peng, Z.; Fiorentino, M.; Beausoleil, R. G. Flat Dielectric Grating Reflectors with Focusing Abilities. *Nat. Photonics* **2010**, *4*, 466–470.
- (12) Yang, Y.; Wang, W.; Moitra, P.; Kravchenko, I. I.; Briggs, D. P.; Valentine, J. Dielectric Meta-Reflectarray for Broadband Linear Polarization Conversion and Optical Vortex Generation. *Nano Lett.* **2014**, *14*, 1394–1399.
- (13) Li, G.; Kang, M.; Chen, S.; Zhang, S.; Pun, E. Y.-B.; Cheah, K. W.; Li, J. Spin-Enabled Plasmonic Metasurfaces for Manipulating Orbital Angular Momentum of Light. *Nano Lett.* **2013**, *13*, 4148–4151.
- (14) Zheng, G.; Mühlender, H.; Kenney, M.; Li, G.; Zentgraf, T.; Zhang, S. Metasurface Holograms Reaching 80% Efficiency. *Nat. Nanotechnol.* **2015**, *10*, 308–312.
- (15) Ni, X.; Kildishev, A. V.; Shalaev, V. M. Metasurface Holograms for Visible Light. *Nat. Commun.* **2013**, *4*, 1038. DOI: 10.1038/ncomms3807.
- (16) Lalanne, P.; Hugonin, J. P.; Chavel, P. Optical Properties of Deep Lamellar Gratings: A Coupled Bloch-Mode Insight. *J. Lightwave Technol.* **2006**, *24*, 2442.
- (17) Yu, N.; Aieta, F.; Genevet, P.; Kats, M. A.; Gaburro, Z.; Capasso, F. A Broadband, Background-Free Quarter-Wave Plate Based on Plasmonic Metasurfaces. *Nano Lett.* **2012**, *12*, 6328–6333.
- (18) Arbabi, A.; Horie, Y.; Bagheri, M.; Faraon, A. Dielectric Metasurfaces for Complete Control of Phase and Polarization with Subwavelength Spatial Resolution and High Transmission. *Nat. Nanotechnol.* **2015**, *10*, 937.
- (19) Ni, X.; Ishii, S.; Kildishev, A. V.; Shalaev, V. M. Ultra-Thin, Planar, Babinet-Inverted Plasmonic Metalenses. *Light: Sci. Appl.* **2013**, *2*, e72.
- (20) Astilean, S.; Lalanne, P.; Chavel, P.; Cambil, E.; Launois, H. High-Efficiency Subwavelength Diffractive Element Patterned in a High-Refractive-Index Material for 633-nm. *Opt. Lett.* **1998**, *23*, 552–554.
- (21) Lalanne, P.; Astilean, S.; Chavel, P.; Cambil, E.; Launois, H. Design and Fabrication of Blazed Binary Diffractive Elements with Sampling Periods Smaller Than the Structural Cutoff. *J. Opt. Soc. Am. A* **1999**, *16*, 1143–1156.
- (22) Yu, Y. F.; Zhu, A. Y.; Paniagua-Domínguez, R.; Fu, Y. H.; Luk'yanchuk, B.; Kuznetsov, A. I. High-Transmission Dielectric Metasurface with  $2\pi$  Phase Control at Visible Wavelengths. *Laser Photonics Rev.* **2015**, *9*, 412–418.
- (23) Lin, D.; Fan, P.; Hasman, E.; Brongersma, M. L. Dielectric Gradient Metasurface Optical Elements. *Science* **2014**, *345*, 298–302.
- (24) Aieta, F.; Genevet, P.; Kats, M. A.; Yu, N.; Blanchard, R.; Gaburro, Z.; Capasso, F. Aberration-Free Ultrathin Flat Lenses and Axicons at Telecom Wavelengths Based on Plasmonic Metasurfaces. *Nano Lett.* **2012**, *12*, 4932–4936.
- (25) Chen, F. T.; Craighead, H. G. Diffractive Phase Elements Based on Two-Dimensional Artificial Dielectrics. *Opt. Lett.* **1995**, *20*, 121–123.
- (26) Chen, F. T.; Craighead, H. G. Diffractive Lens Fabricated with Mostly Zeroth-Order Gratings. *Opt. Lett.* **1996**, *21*, 177–179.
- (27) Stork, W.; Streibl, N.; Haidner, H.; Kipfer, P. Artificial Distributed-Index Media Fabricated by Zero-Order Gratings. *Opt. Lett.* **1991**, *16*, 1921–1923.
- (28) Li, Z.; Palacios, E.; Butun, S.; Aydin, K. Visible-Frequency Metasurfaces for Broadband Anomalous Reflection and High-Efficiency Spectrum Splitting. *Nano Lett.* **2015**, *15*, 1615–1621.
- (29) Aieta, F.; Kats, M. A.; Genevet, P.; Capasso, F. Multiwavelength Achromatic Metasurfaces by Dispersive Phase Compensation. *Science* **2015**, *347*, 1342–1345.
- (30) Zhan, Q. Cylindrical Vector Beams: From Mathematical Concepts to Applications. *Adv. Opt. Photonics* **2009**, *1*, 1–57.
- (31) Zheludev, N. I.; Kivshar, Y. S. From Metamaterials to Metadevices. *Nat. Mater.* **2012**, *11*, 917–924.
- (32) Sorger Volker, J.; Lanzillotti-Kimura Norberto, D.; Ma, R.-M.; Zhang, X. Ultra-Compact Silicon Nanophotonic Modulator with Broadband Response. *Nanophotonics* **2012**, *1*, 17.
- (33) Dalton, L. R.; Sullivan, P. A.; Bale, D. H. Electric Field Poled Organic Electro-Optic Materials: State of the Art and Future Prospects. *Chem. Rev. (Washington, DC, U. S.)* **2010**, *110*, 25–55.
- (34) Feigenbaum, E.; Diest, K.; Atwater, H. A. Unity-Order Index Change in Transparent Conducting Oxides at Visible Frequencies. *Nano Lett.* **2010**, *10*, 2111–2116.
- (35) Iyer, P. P.; Butakov, N. A.; Schuller, J. A. Reconfigurable Semiconductor Phased-Array Metasurfaces. *ACS Photonics* **2015**, *2*, 1077–1084.
- (36) Thompson, K. P.; Rolland, J. P. Freeform Optical Surfaces: A Revolution in Imaging Optical Design. *Opt. Photonics News* **2012**, *23*, 30–35.